Research in Astronomy and Astrophysics, 25:075016 (15pp), 2025 July

https://doi.org/10.1088/1674-4527/adda7c
CSTR: 32081.14.RAA.adda7c

Distance Estimation of the High-velocity Cloud Anti-center Shell

Yu-Ting Wang (王雨亭)[1,2], Chao Liu (刘超)[1,2,3], and Zhi-Yu Zhang (张智昱)[4,5]
[1] Key Laboratory of Space Astronomy and Technology, National Astronomical Observatories, CAS, Beijing 100101, China; liuchao@nao.cas.cn
[2] University of Chinese Academy of Sciences, Beijing 100049, China
[3] Zhejiang Lab, Hangzhou 311121, China
[4] School of Astronomy and Space Science, Nanjing University, Nanjing 210023, China
[5] Key Laboratory of Modern Astronomy and Astrophysics (Nanjing University), Ministry of Education, Nanjing 210023, China
Received 2024 December 11; revised 2025 April 25; accepted 2025 May 15; published 2025 June 17

Abstract

High-velocity clouds (HVCs) are interstellar gas clouds whose velocities are incompatible with Galactic rotation. Since the first discovery of HVCs in 1963, their origins have been debated for decades but are still not settled down, because of the lack of vital parameters of HVCs, e.g., the distance. In this work, we determined the distance to the HVC, namely the Anti-center Shell (ACS). We trace the ACS with extinction derived from K-giant stars with known distances and with the diffuse interstellar band (DIB) feature at 5780 Å fitted on spectra of O- and B-type stars with distance. As a result, we provide a lower limit distance of ACS as ∼8 kpc, which extends the lower limit outward by approximately 4 kpc compared to previous work. A byproduct of the DIB method is that we detected a bar-shaped structure with an unusually high positive line-of-sight velocity. Its shape extends along the $(l, b) = (155, -5)^\circ$ sight-line and shows a slightly increasing trend in equivalent width and velocity as the distance increases.

Key words: galaxies: ISM – Galaxy: kinematics and dynamics – ISM: clouds – (ISM:) dust, extinction – ISM: lines and bands

1. Introduction

High-velocity clouds (HVCs) are neutral or ionized gas clouds in the vicinity of the Milky Way (MW) that are characterized by velocities incompatible with Galactic differential rotation (Wakker & van Woerden 1997). Traditionally, astronomers selected out HVCs by applying a crude and invariable cut of line-of-sight velocity in the local standard of rest (LSR) reference framework, such as $|v_{\rm LSR}| \gtrsim 90\,{\rm km\ s^{-1}}$. After that, an improved definition was proposed by Wakker (1991) who introduced a so-called deviation velocity $v_{\rm dev} = 50\,{\rm km\ s^{-1}}$ to characterize HVCs as deviating by a fixed velocity separation from the maximally permissible velocity of the Galactic disk in a given direction. Recently, Westmeier (2018) assumed a simple, cylindrical model of the Galactic disk with a disk radius of 20 kpc, a disk height of 5 kpc, and a deviation speed of $v_{\rm dev} = 70\,{\rm km\ s^{-1}}$ to produce velocity masks to filter out disk component based on the all-sky H I4π survey (HI4PI; HI4PI Collaboration et al. 2016), a database for Galactic H I emission. The map of Westmeier (2018) offers a comprehensive and high-resolution vision of HVCs and thus becomes the cornerstone of this field.

Apart from H I 21 cm observations, another observational technique for HVCs that deserves equal attention is the absorption-line method, by which HVCs can be reached by absorption toward bright background halo stars or quasars, mostly at ultraviolet wavelengths (Smoker et al. 2011; Marasco et al. 2022). While 21 cm H I observations provide us a uniform all-sky HVC map (Westmeier 2018), the absorption-line method, on the other hand, can probe much lower hydrogen column density and detect ionized materials in the HVCs (e.g., Sembach et al. 2000; Lehner et al. 2001; Sembach et al. 2003).

Despite nearly six decades having passed since the initial detection of the HVC in 1963 (Muller et al. 1963), the enigmatic origin of them persists as an unresolved problem. Based on current observations, HVCs require at least three formation mechanisms: one for the Magellanic Stream and its associated clouds, one for the Outer Arm Extension, and one for the rest of the HVCs. Currently, existing hypotheses can be roughly categorized into four groups according to the locations of HVCs:

(1) The HVCs are situated in the solar neighborhood, indicating that they originated from nearby supernova explosions (e.g., Heiles 1979);
(2) The HVCs are gas at the disk-halo interface, indicating the transfer of gas between these two regions (e.g., Marasco et al. 2022);
(3) The HVCs are situated in the Outer Galaxy, e.g., as the polar ring wrapping our MW or as gas stripped or ejected from dwarf galaxies (e.g., Davies 1972);
(4) The HVCs stem from an even more distant place, as gas from the Local Group or as infalling intergalactic matter (e.g., Verschuur 1969).

Intriguing as the origin theories are, it is vital to pin down the fundamental properties (e.g., distance, metallicity, and 3D kinematics) of HVCs if we want to figure out the detailed origin mechanisms. Distance measurement is critical since it helps to distinguish which categories the birth of HVCs might fall into, as well as to quantify their fundamental physical properties, several of which directly scale with the distance (e.g., total mass, size, density, pressure, Wakker & van Woerden 1997). However, distance determination for HVCs is challenging. The most used method is the absorption-line method (Schwarz et al. 1995). Absorption line features produced by HVCs can be explored with spectroscopic observations of background objects with known distances, leading us to metallicity, velocity, and constraints on distance (upper limit and lower limit). Up until now, a considerable volume of work using the absorption-line method has been published (e.g., Schwarz et al. 1995; Ryans et al. 1997; Wakker 2001; Smoker et al. 2006; Thom et al. 2006; Wakker et al. 2007, 2008; Thom et al. 2008; Lehner & Howk 2010; Smoker et al. 2011; Tripp & Song 2012; Peek et al. 2016; Lehner et al. 2022). However, the absorption-line method has trouble giving a precise distance to the HVCs because it suffers from the limitation of sparsely distributed tracer stars (Marasco et al. 2022) due to the deficiency of ultraviolet band spectra.

In this paper, we intend to use interstellar extinction to trace the HVC Anti-center Shell (ACS) and constrain its distance. When starlight penetrates gas, dust, etc., its energy will be attenuated by absorption or scattering, called interstellar extinction. Generally, the atomic cloud regions have higher densities than the ambient medium. Consequently, the extinction in the HVC sight line would increase more than in the surroundings. The location of the extinction excess will reveal our distance to the cloud. Yan et al. (2019, 2021), Zucker et al. (2019), Wang et al. (2020) have all successfully measured the distance to various types of objects, such as molecular clouds, supernova remnants (SNRs), etc., using the extinction method. Numerous and extensively distributed K giants in the MW, which are our extinction tracers, can be helpful to derive much more precise distances. Hence, they can be used to probe down to the inner three-dimensional structure of the ACS with the extinction method. Meanwhile, to take advantage of the velocity information in the H I 21 cm emission observation, we take the Diffuse Interstellar Band (DIB) feature as an auxiliary tracer to verify the position of the very step-like pattern in the distance-extinction plot independently caused by ACS.

The paper is structured as follows. In Section 2, we describe the sample we used and our filtering strategy. Section 3 describes how we utilized extinction and DIBs to locate the HVC ACS. Section 4 presents the main results from the above methods, in which we provide the lower distance limit of ACS and report a newly discovered positive velocity high-velocity DIB clump. We further discuss these results in Section 5. The final section summarizes our main findings and discusses possible future improvements of this work.

2. Data Collection

2.1. Cloud Properties

The ACS is a shell-like low-latitude HVC located in the direction opposite to the Galactic center from our solar system (Westmeier 2018). This shell has a $\sim 40^\circ$ diameter and a mean line-of-sight velocity in the LSR of ~ -100 km s^{-1}. The ACS is chosen as our target because: (1) It is located in the anti-center region with low Galactic latitude, making it plausible to be found within 6 kpc from the Sun, where Gaia distance data stays valid; (2) Previous work suggested that ACS might require independent origin theory (Wakker & van Woerden 1997). Distance measurement can constrain its way of formation and provide insights into its interactions with the surrounding environment.

2.2. Spectroscopically Identified Parameters of K Giants from LAMOST Data Release 5

We employed interstellar extinction to illustrate the spatial distribution of the ACS since dust and gas particles in the cloud are both extinction generators (Draine 2003). K-giant stars are commonly used tracers in extinction/reddening studies because of their brightness and abundance, making them substantially observed in the MW (Xue et al. 2016).

The Guo Shou Jing Telescope (LAMOST) is a 4 m special quasi-meridian reflecting Schmidt telescope located at Xinglong Observatory of National Astronomical Observatories, Chinese Academy of Sciences (Cui et al. 2012). It recently completed its twelfth data release and enabled global access to its tenth release of data. Till today, it has released an unprecedentedly large amount of low- and mid- resolution stellar spectra of over 17,000,000.[6]

Xu et al. (2020) compiled a catalog of K-type giant stars using LAMOST DR5, which aligns well with the objectives of this study. Atmospheric parameters (e.g., effective temperature $T_{\rm eff}$, and surface gravity $\log g$) determined using Stellar LAbel Machine (SLAM; Zhang et al. 2020) can be extracted from this catalog. According to Xu et al. (2020), K-giant stars in LAMOST were selected following the criteria presented in Liu et al. (2014):

$$\begin{aligned}&(4000 < T_{\rm eff} < 4600\ \mathrm{K},\ \log g < 3.5)\\&\quad\vee(4600 < T_{\rm eff} < 5600\ \mathrm{K},\ \log g < 4.0)\end{aligned} \tag{1}$$

Here, $T_{\rm eff}$ and $\log g$ stand for effective temperature and surface gravity, respectively. They also conducted a metallicity cut of [M/H] > -1.2 to avoid halo stars, which nicely favors

[6] The information can be found on their official website: https://www.lamost.org/public/?locale=en.

our work since this will alleviate the metallicity's influence on color.

We additionally adopt a quality cut on the g-band signal-to-noise ratio *snrg* to ensure the reliability of the effective temperature $T_{\rm eff}$:

$$snrg > 15. \tag{2}$$

To ensure a reliable statistical analysis, the number of sources needs to be large enough in each 100 K wide effective temperature bin. Therefore, we only kept stars in the temperature range:

$$4000 < T_{\rm eff} < 5300\ {\rm K}. \tag{3}$$

2.3. 2MASS All Sky Data Release: Point Source Catalog

The Two Micron All Sky Survey (2MASS) is an all-sky survey using two 1.3 m telescopes located at Mount Hopkins, Arizona, and Cerro Tololo, Chile. This survey encompasses three near-infrared passbands, namely J, H, and $K_{\rm S}$. The photometry was verified to have approximately 0.02 mag accuracy (Skrutskie et al. 2006).

We adopted the J- and $K_{\rm S}$-band photometry from the 2MASS data to derive the color index $J - K_{\rm S}$. We made a cut on the photometric quality flag `ph_qual` to keep only the sources with the flag value `A`. The value of `ph_qual` is set based on signal-to-noise ratio, measurement quality, and detection statistics. Besides, a `cc_flg` screening was also included to remove sources probably contaminated by proximity. The precise description of these flags can be retrieved at.[7]

$$\begin{aligned} \texttt{ph\_qual} &= \text{“}A * A'' \\ \texttt{cc\_flg} &= \text{“}0 * 0'' \end{aligned} \tag{4}$$

Here, the asterisks mean that we did not put any constraint on the photometry quality of the H-band data.

2.4. Bailor-Jones' Distance Estimation Based on Gaia EDR3

We adopted the distance estimated in the literature (Bailer-Jones et al. 2021), which is based on the Gaia EDR3 Catalog. This work estimated distances for 1.47 billion objects in Gaia EDR3 using a Bayesian approach based on a prior built from a three-dimensional Galactic model that considered interstellar extinction and the magnitude limit of Gaia. Two types of distance are provided alongside the article. The geometric one only used Gaia EDR3 parallax and the geometric prior above. The second, photogeometric distance, added color and apparent magnitude to give extra constraints. We chose to use the geometric distance `rgeo` in this article to avoid inviting color and magnitude reliance.

Bailer-Jones et al. (2021) recommended using the various quality fields in the main Gaia catalog of EDR3 for quality filtering purposes, rather than using the flags in Bailer-Jones et al. (2021) to select high-quality distance estimates. We used the following constraints in this study:

$$\begin{aligned} &\texttt{ruwe} < 1.4, \\ &\texttt{parallax\_over\_error} > 5. \end{aligned} \tag{5}$$

2.5. Diffuse Interstellar Band (DIB) Feature as the Cloud Tracer

2.5.1. Catalog of 16,002 O- and B-type Stars from LAMOST

The DIBs are a large set of absorption features that arise in interstellar gas (Herbig 1995). In this work, we focused only on the absorption at about 5780 Å, which has been validated as highly correlated with the intensity of interstellar reddening and H I 21 cm emission (Herbig 1995; Lan et al. 2015). It is convenient to extract the DIB λ5780 from the spectra of O- and B-type stars since they do not show many other stellar features at the red end.

The catalog of 16,002 O- and B-type stars from LAMOST by Xiang et al. (2021) is perfectly suited for this process, so we selected the O- and B-type stars in the ACS direction from their catalog and downloaded corresponding low-resolution spectra from LAMOST Data Release 8.[8]

3. Method

3.1. Extinction as the Cloud Tracer

Because the attenuation of light by interstellar extinction is wavelength-dependent, which is more efficient in the bluer wavelengths, stellar lights are typically reddened when they penetrate through the interstellar medium (Draine 2003). The interstellar extinction (A_λ) and reddening (characterized by the color excess $E(\lambda_1 - \lambda_2) = A_{\lambda_1} - A_{\lambda_2}$) are therefore highly correlated, and their relationship can be demonstrated by the extinction law (Wang & Chen 2019). Given the definition of interstellar reddening, we calculated the color excess $E(J - K_{\rm S})$ of the K-giant stars with the equation:

$$E(J - K_{\rm S}) = (J - K_{\rm S}) - (J - K_{\rm S})_0, \tag{6}$$

where $(J - K_{\rm S})$ means the observational color, and $(J - K_{\rm S})_0$ is the intrinsic color of stars.

We determined the intrinsic color $(J - K_{\rm S})_0$ by assuming that the color of the bluest star at a specific effective temperature is the intrinsic color at this temperature. According to Ducati et al. (2001), Wang & Jiang (2014), Xue et al. (2016), for tracer stars distributing sufficiently broad in space, the bluest stars can be treated as a reference without extinction. In practice, we divided the K-giant stars into 100-K wide

[7] https://irsa.ipac.caltech.edu/data/2MASS/docs/releases/allsky/doc/explsup.html

[8] https://www.lamost.org/public/

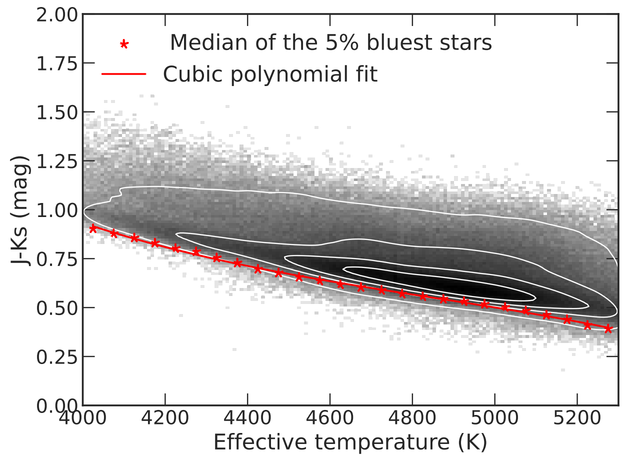

Figure 1. All the K-giant samples plotted on the $T_{\rm eff} - (J - K_{\rm S})$ diagram. The red asterisks denote the median color of the 5% bluest stars in each $T_{\rm eff}$ bin. The red curve shows the cubic polynomial fitting result to the red asterisks, which was considered as the derived $T_{\rm eff} - (J - K_{\rm S})_0$ relation.

effective temperature bins and computed the median color of the top 5% bluest stars in each bin. After that, we fitted the $\{T_{\rm eff},\quad (J - K_{\rm S})_0\}_i$ relation with a cubic polynomial, obtaining an effective temperature-intrinsic color relation as in Equation (7). The obtained blue effective temperature-intrinsic color relation is plotted in Figure 1. With this relation, we can gain the reddening for every star with Equation (6).

To extract the extinction excess caused by ACS alone, we first sorted out tracer stars projecting inside the cloud profile and also those surrounding the cloud as a control group. By comparing the two, the cloud signal can be highlighted. In this part, we exploited the all-sky HVC map constructed by Westmeier (2018) to create an ACS mask. Stars located within the 21 cm H I emission region of the ACS are assigned to the "on-cloud" group, while others are assigned to the "off-cloud" control group. The illustration of cloud profile is shown in Figure 2, color-coded by its logarithm H I column density and radial velocity in LSR.

$$(J - K_S)_0 = -3.94 \times 10^{-11} T_{\rm eff}^3 + 6.94 \times 10^{-7} T_{\rm eff}^2 - 4.26 \times 10^{-3} T_{\rm eff} + 9.36 \tag{7}$$

Now we have stars that distribute merely "on" the cloud, enabling us to trace the extinction variation along the sight line of ACS. The next step involves classifying these stars into distinct distance intervals. Here, we chose 200 pc as the bin size, a value that strikes a balance between maintaining acceptable measurement errors and ensuring noticeable resolution of the fine structure within the variation curve. Through shifting our temperature-intrinsic color relation line (also referred to as the "bluest edge" in the following text) to minimize the difference between the stars in each distance bin in the distance-color plot and the shifted bluest edge, we obtain the mean reddening suffered by these tracers, being the amount

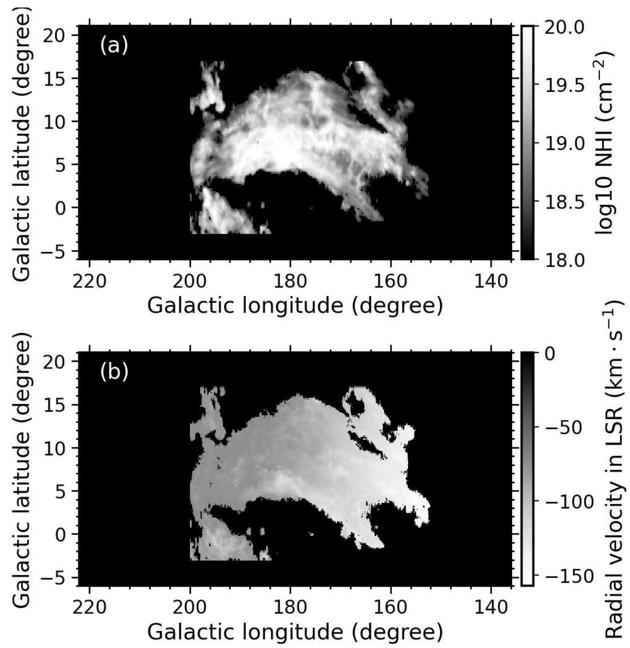

Figure 2. H I 21 cm emission map of Anti-center Shell (ACS) from HI4PI survey. The color map shows the column density (a) and mean radial velocity (b) distribution of neutral hydrogen at each sight line on the cloud.

of displacement we applied to the bluest edge. The resulting Figure 3 illustrates the obtained extinction variation curve, with the error bars in the graph reflecting the comprehensive uncertainty, including the uncertainty of the blue edge, the observational uncertainty of distance measurement, J-band and $K_{\rm S}$-band photometry, and the emerged Poisson error when binning the data into sight line and distance bins. The detailed error estimation process for the extinction method is described in the Appendix.

The ACS is an HVC in the low-latitude region, which is uncommon among the HVC family (Westmeier 2018). This feature complicates the recognition process for the exact step-like pattern that ACS produces because the presence of the Galactic disk and the extensive dust in it will lead to a large amount of additional foreground/background extinction. As depicted in Figure 3, there are several "stairs" as the distance increases, resulting from different sub-structures. Consequently, including a control group in the study is necessary. The control group encompasses a larger area beyond the cloud and is confined within Galactic longitude $\in [135, 220]^\circ$ and Galactic latitude $\in [-5, 25]^\circ$. To avoid excessive information loss caused by averaging over such a large region, we grouped the samples based on latitude. We split the on-cloud and off-cloud groups into low-latitude, medium-latitude, and high-latitude parts, respectively, and compared the derived extinction variation within the same latitudes, as illustrated in Figure 4. The major difference in the overall growth of $E(J - K_S)$ among these curves originates from global

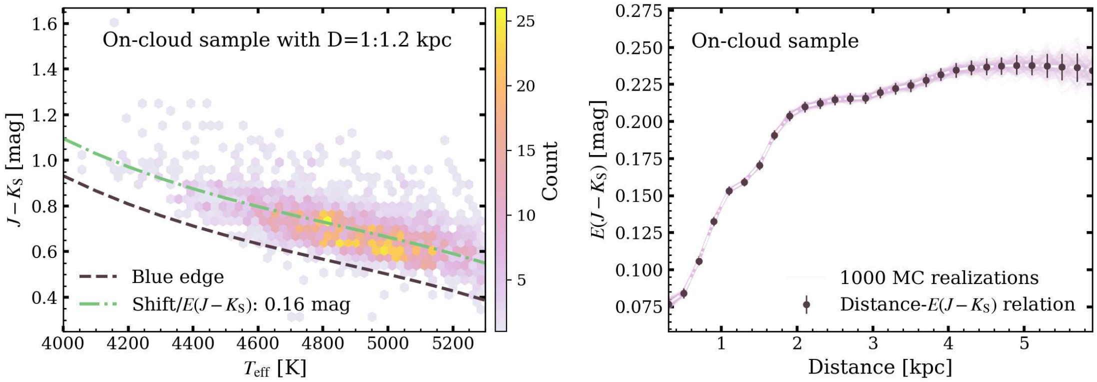

Figure 3. (Left) Give an example of how the average reddening of one distance bin (from 1 to 1.2 kpc) is fitted. The hexagonal binning plot shows the number density distribution of the stars from 1 to 1.2 kpc in the temperature-color plane. The black dashed line illustrates the blue edge that we derived before. The green dotted-dashed line illustrates the best-fitted shift amount for the stars in the plot. (Right) We bin the on-cloud sample from 0 to 6 kpc with a distance width of 0.2 kpc. We resample the distance, temperature, and color $J - K_S$ according to their observational uncertainties, and fit for the average $E(J - K_S)$ of each distance bin for 1000 runs. The MC results are plotted with pink solid lines. The median distance-$E(J - K_S)$ relation is plotted with black dots and white lines, with the uncertainty caused by the measurement of the blue edge already added in the error bars.

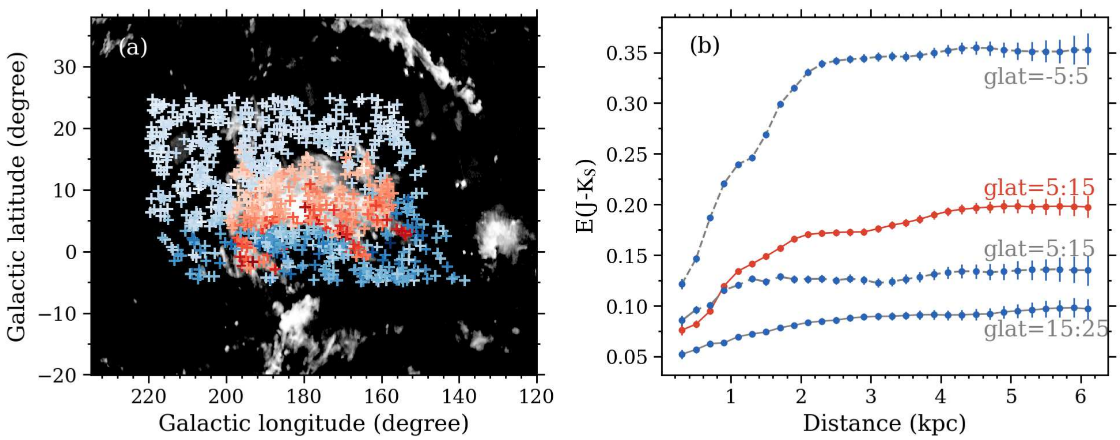

Figure 4. (a) Illustration of the target regions of the four curves in Panel (b). The color intensity of red and blue represents the magnitude of reddening, respectively, for the stars on-cloud and off-cloud. (b) Mean reddening varies with distance along four different sight lines. The curve produced by stars on-cloud and at Galactic latitude $\in[5, 15]^\circ$ is plotted with red crosses and a red solid line. The curves made by low-latitude, medium-latitude, and high-latitude off-cloud stars are drawn by blue crosses and gray dashed, solid, and dashed–dotted lines, respectively.

extinction variation in the MW. Detailed analysis will be performed in Section 4.

3.2. Diffuse Interstellar Band (DIB) Feature as the Cloud Tracer

From the spectra of O- and B-type stars, we can extract the line center and equivalent width of the interstellar absorption feature at the location of each tracer by straightforward Gaussian fitting, and the continuum is estimated and deducted using the iterating method described in Zhao et al. (2021).

The iterative continuum fitting process from Zhao et al. (2021) began by fitting the $\lambda5780$ local spectrum with a second-order polynomial and calculating the standard deviation of flux differences between individual pixels and the fit curve. Pixels above the curve were replaced by the corresponding points on the fitting curve if they exceeded 5σ, while those below were replaced at 0.5σ. The process was iteratively repeated 20 times using the remaining valid pixels and replacement points, with the final polynomial fit serving as the continuum for renormalization.

Line center can be converted into the line-of-sight velocity (also radial velocity above) of DIB $\lambda5780$ carrier, while the absorption intensity, quantified by equivalent width, has been established by previous studies to exhibit a strong correlation with both the level of reddening and the 21 cm H I emission (Herbig 1995; Lan et al. 2015). Consequently, this method not only allows us to construct a distance-reddening plot, which in this case takes the form of a distance-equivalent width plot, but also introduces an additional crucial dimension, radial velocity. The inclusion of velocity measurements enables us to identify signals associated with HVCs in the H I observations.

After fitting the continuum and line center, we performed a series of quality cuts to retain measurements with reliable DIB λ5780 detection. First of all, we required the spectrum signal-to-noise ratio *snrg* > 35 to guarantee that the quality of our spectra was good enough for DIB λ5780 measurement. We also used the ratio of equivalent width value to equivalent width error to keep only `EW5780/EW5780_err` > 4 as "detection" of DIB λ5780 feature (otherwise, as "non-detection"). Finally, we checked our data on the equivalent width-reddening plot (EW $- E(B-V)$), excluding the points that deviate explicitly from a linear relation. Specifically, we fitted the EW $- E(B-V)$ distribution to a linear relation and calculated the standard deviation σ of our data from this linear relation. Data points deviating more than 3σ from this relation were excluded.

To filter out DIB λ5780 detections with velocities incompatible with Galactic differential rotation (also referred to as high-velocity DIBs, or HV-DIBs later), we applied the method employed by Westmeier (2018) to screen out HVCs in H I 21 cm emission database. We adopted the rotation curve by Clemens (1985) and projected this rotation velocity onto the line-of-sight direction using Equation (3) in Westmeier (2018):

$$v_{\rm proj} = \left[v_{\rm rot}(r_{\rm xy}) \frac{r_{\odot}}{r_{\rm xy}} \right] \sin l \cdot \cos b \quad (8)$$

where $r_{\rm xy}$ equals the projection length of the Galactocentric distance onto the xy-defined Galactic plane.

Assuming that the Galactic disk is a cylinder with $r_{\rm max} = 20$ kpc and $|z_{\rm max}| = 5$ kpc (the same values as set by Westmeier 2018), we can calculate the distance range $[0, d_{\rm max}]$ encountered between the Sun and the boundary of this cylindrical disk model at certain (l, b).

Now we can obtain the projected velocity range of MW rotation at any given (l, b). We considered the DIB λ5780 with a radial velocity deviating more than 70 km s^{-1} from this range as HV-DIB, and the uncertainty in velocity determination is taken into account by Equation (9). The result is shown in Figure 5. The gray dots are all reliable DIB measurements selected with the above criteria. The shaded area represents the velocity range permitted by Galactic differential rotation. Normal velocity dispersion on the disk is included in the deviation velocity $v_{\rm dev} = 70$ km s^{-1}. HV-DIB measurements, i.e., DIBs with anomaly velocity, are drawn with asterisks and are color-coded by their equivalent widths.

$$v + \sigma_v < v_{\rm proj,min} - 70 \quad \text{or} \quad v - \sigma_v > v_{\rm proj,max} + 70 \quad (9)$$

It is easy to notice that there exist both negative velocity HV-DIBs and positive velocity ones in Figure 5. ACS is a negative velocity HVC, which means it has a movement toward us, so we should primarily check these negative

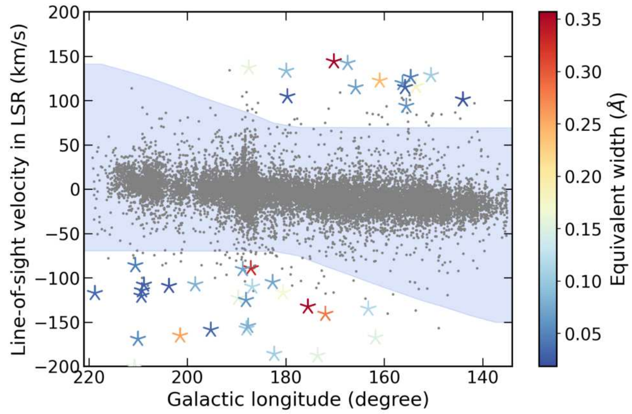

Figure 5. DIB λ5780 measurements in the Galactic longitude-radial velocity plot. The gray dots are all reliable DIB measurements selected with criteria listed in Section 3.2. The shaded area implies the velocity range permitted by Galactic differential rotation. Normal velocity dispersion on the disk is included in the deviation velocity $v_{\rm dev} = 70$ km s^{-1}. HV-DIB measurements, i.e., DIBs with anomaly velocity, are marked with asterisks and color-coded by their equivalent widths.

velocity HV-DIB points in space to see if they are statistically clustered to form a sub-structure like ACS. This will be discussed in Section 4.

4. Results

This part will discuss the main results from the extinction method and the DIB method in Section 3.

4.1. Bimodal Distribution in Distance-Reddening Scatter Plot

In Figure 3, the curve drawn with tracer stars projected on-cloud has several step-like patterns on it. However, it seems that none of them is solely displayed in the on-cloud plot according to Figure 4. The first two significant extinction steps at 1 kpc and 2 kpc are probably caused by the Local Arm and the Perseus Arm (Xu et al. 2023).

Since averaging reddening $E(J - K_S)$ in Figure 4 may wipe out essential information, we again calculated the individual reddening of all K-giant stars and produced a scatter plot in Figure 6. There are two separated components in both plots: a high-extinction one probably stemming from sight lines going through the dusty Galactic disk, and a low-extinction component going through the higher-latitude low-density regime.

We manually separated these components in Figure 6 and illustrated their distribution in Galactic longitude-galactic latitude (glon-glat) space in Figure 7. It is evident that the high-extinction components, both in the on-cloud and off-cloud groups, are predominantly concentrated in low-latitude regions, which are likely associated with the structure of the Galactic disk. In contrast, low-extinction ones are located at higher latitudes. This spatial distribution provides further

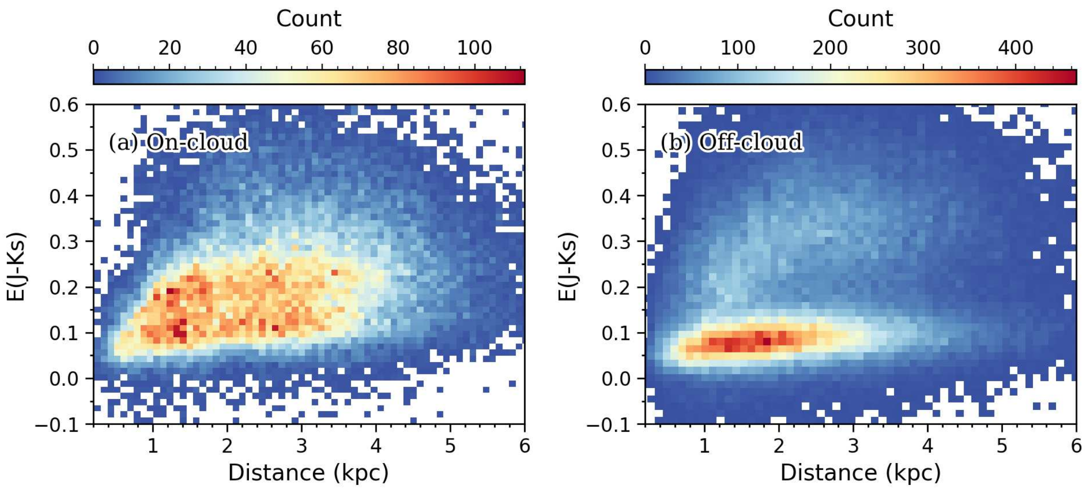

Figure 6. Individual reddening of all K-giant stars (a) on-cloud; (b) off-cloud. There are two separated components in both plots: a high-extinction one probably stemming from sight lines going through the dusty Galactic disk, and a low-extinction component going through higher-latitude low-density halo.

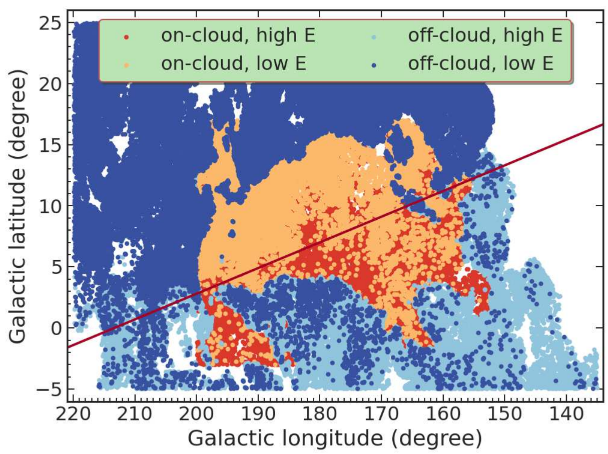

Figure 7. Spatial distribution of different extinction modes. Red dots denote the high-extinction component on-cloud, orange ones denote the low-extinction component on-cloud, and light blue ones the high-extinction component off-cloud, deep blue ones the low-extinction component off-cloud. The red solid line shows the rough boundary among each component, which is consistent with the shape of the dust disk's warp of our Milky Way.

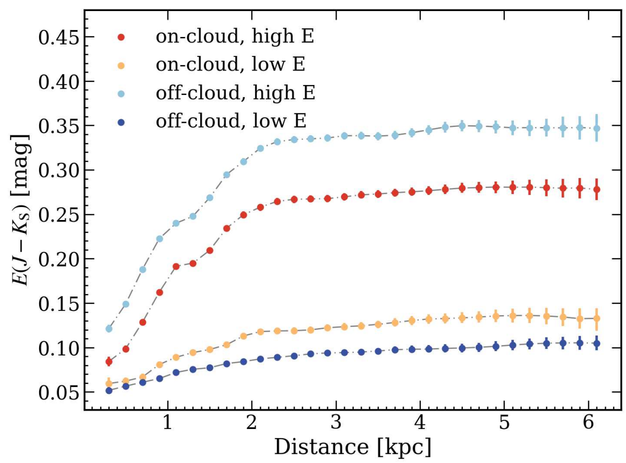

Figure 8. Distance-average reddening relation for each extinction mode reclassified in spatial distribution. We use the same color strategy as that in Figure 7.

support for our explanation regarding the origin of the bimodal pattern depicted in Figure 6. We used a solid red line to specify the approximate boundary between the low-extinction and the high-extinction components in Figure 7. The edge between the high and the low-extinction regime appears to be tilted, potentially indicating the presence of a warp in the interstellar dust distribution within our Galaxy (Freudenreich et al. 1994).

We then regrouped these components according to their spatial distribution relative to the solid red line in Figure 7 and calculated the mean reddening $E(J - K_S)$ in distance bins to extract the primary trend of variation. We used the same color strategy in Figure 7 to draw the distance-mean reddening curve of the spatially reclassified components in Figure 8. In principle, the two low-extinction groups allow a better chance to show ACS with a step in the reddening-distance plot because the contamination from the disk can be avoided there. However, we do not find a significant difference beyond 2 kpc. The difference at around 1–2 kpc between these two low-extinction curves is probably due to the residual impact of the Local Arm and the Perseus Arm, instead of the ACS.

4.2. Negative Velocity HV-DIBs and Distance Lower Limit of Anti-center Shell (ACS)

With extinction and distance, we can only identify the step produced by ACS through comparisons of extinction variation in different regions. This method will be less effective when the

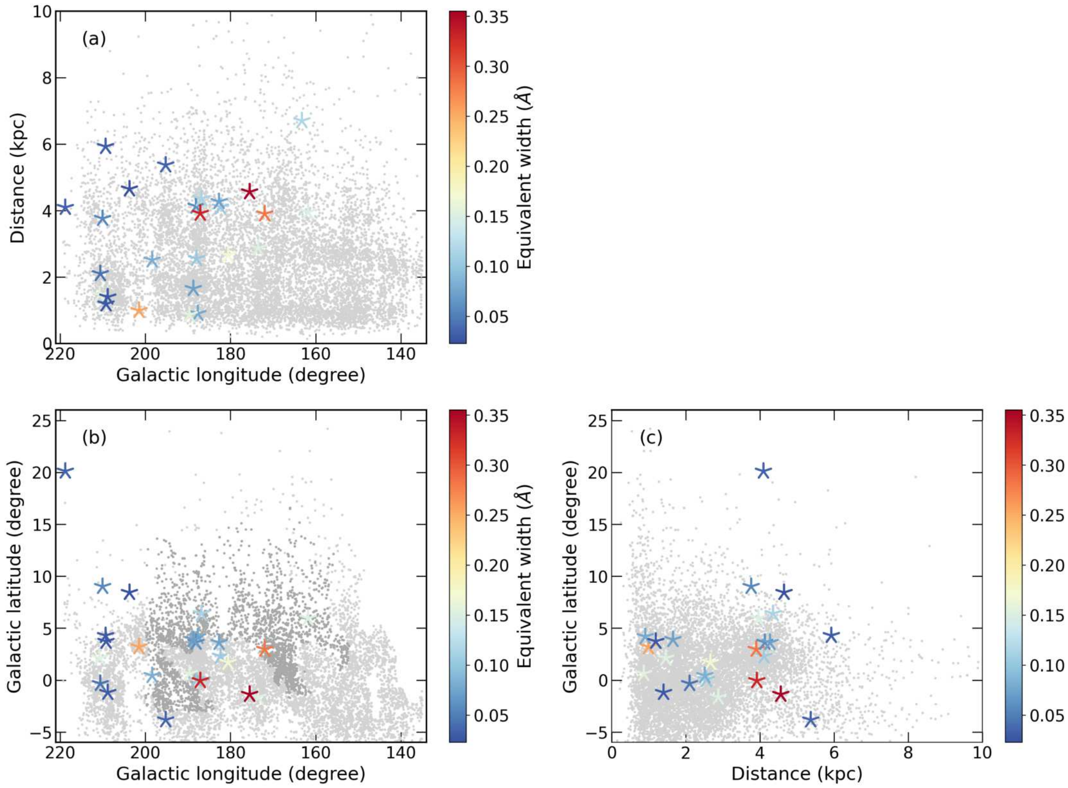

Figure 9. Three-dimensional positions of HV-DIBs with negative velocity. We used the distance of our O- and B-type star tracers accomplished by Bailer-Jones et al. (2021). HV-DIBs are color-coded by their equivalent width. Light gray dots on the background show all reliable DIB measurements, and dark gray dots in (b) emphasize the cloud area.

signal is weak. However, we are able to obtain the velocity of DIB carriers at each point in the second method and screen out anomaly velocities incompatible with the Galactic disk. Since the ACS is a negative velocity HVC, we first inspected the negative velocity HV-DIBs in Figure 5 to see if they display any statistical structure in space. In Figure 9, HV-DIBs with negative velocity do not show any clustering behavior at the same position as ACS' 21 cm H I emission in three-dimensional space, which means there is no significant signal from ACS in the DIB measurements.

Non-detection of the cloud signal allows us to give the lower limit of the ACS distance. We then dropped the stars with unreliable Bailor-Jones' distances whose signal-to-noise (SNR) values are smaller than one (note that we defined SNR here as `D/(D_HIGH-D_LOW)`). Eventually, we found the star with Bailor-Jones' distance 8.1 ± 1.8 kpc to provide the final distance lower limit.

5. Discussion

5.1. Stacked Spectra for the Diffuse Interstellar Band λ5780 in the Cloud Region

In this section, we stacked the spectra of O- and B-type stars projected onto three selected regions (shown in Figure 10) to enhance potential ACS signals. Prior to stacking, each spectrum was normalized by dividing by its continuum. The on-cloud experimental group, marked with green crosses in Figure 10, excludes stars below the tilted line in Figure 7 to minimize disk contamination. Two off-cloud control groups, marked with blue and orange crosses, were selected at sufficient distances from the ACS cloud to avoid potential interference from its outer ionized regions. The continuum was calculated following the methodology described in Section 3.2 (Zhao et al. 2021). Figure 11 presents the results: the green solid line shows the stacked spectra of stars in the cloud region, while blue and orange dashed lines represent the stacked spectra from the off-cloud control regions.

As shown in Figure 11, the DIB λ5780 peaks align across all three regions, with no bimodal structure observed in the negative velocity (left-wing) portion of the absorption feature for the experimental group stars. While the DIB λ5797 feature in the on-cloud sample spectrum appears shifted toward more negative velocities, Gaussian profile fitting yields a velocity of $-32.6\,\mathrm{km\ s^{-1}}$. This value is significantly different from the ACS velocity of $v_{\mathrm{LSR}} \sim -100\,\mathrm{km\ s^{-1}}$. These results further support our non-detection of ACS using the DIB method.

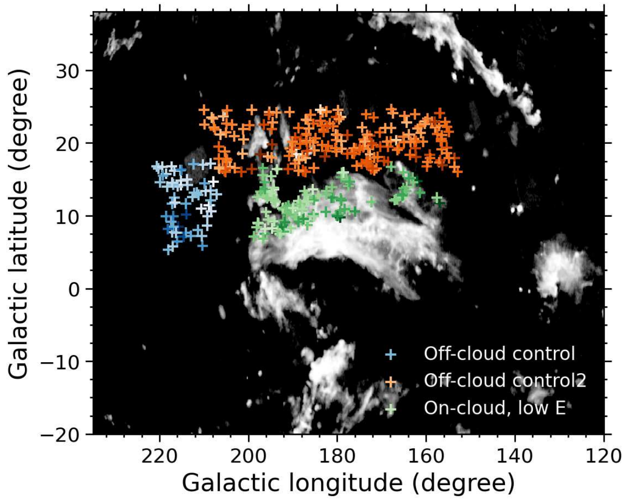

Figure 10. Illustration of the three regions used for stacking DIB $\lambda 5780$ spectra. Green crosses indicate O- and B-type stars projected onto the ACS cloud region, while blue and orange crosses denote stars in the off-cloud control regions. The color intensity of green, blue and orange represents the magnitude of reddening, respectively, for the stars in the three groups.

5.2. Explanations for Non-detection of the Anti-center Shell

Non-detection of the negative velocity HVC ACS in both the extinction method and the DIB method can be interpreted as a distance limitation of our tracers, meaning that we can deduce the lower limit of the HVC in this scenario. Non-detection of the ACS by our methods can also be caused by the sensitivity of our methods. The signal of ACS may be concealed by the strong component of the Galactic disk. Another explanation for our non-detection might be that the neutral hydrogen and dust in the ACS are not sufficient to cause a remarkable extinction excess. We can see from Figure 2 that the densest part of the cloud has an H I column density of $\log_{10}(N_{\rm H\,I}) \sim 20$, and according to the $E(B-V) - N_{H\,\rm I}$ relation in Figure 11 of Lan et al. (2015), this column density corresponds to negligible $E(B-V)$. Chances are that this cloud is also too hot to harbor dust and DIB carriers to produce significant enough extinction and cause the malfunction of our methods. This explanation is based on that the HVC ACS' composition is similar to that of the all-sky cloud-averaged in the MW, allowing us to apply the $N_{\rm H}\,\rm I - E(B-V)$ relation in Lan et al. (2015), which is not necessarily true.

5.3. Positive Velocity HV-DIBs

Though negative velocity HV-DIBs do not show any statistically clustering behavior, positive ones do present some intriguing clues. In Figure 12, DIBs at $(l, b) = (155, -5)^\circ$ show clustering characteristics in all three plots, clumpy-shaped in the glon-glat plot and bar-shaped in plots relevant to distance. We revisited our spectrum fitting results of these positive velocity HV-DIBs and retained those good-fitting ones to draw in the X–Y plane in Figure 13 to see the integral variation in velocity and equivalent width along the strip-like structure. We plotted the eye check results of the spectrum fitting of stars with positive velocity HV-DIB detection in Figure 14. The reliable measurements are shown on the left side, while the unreliable ones on the right side.

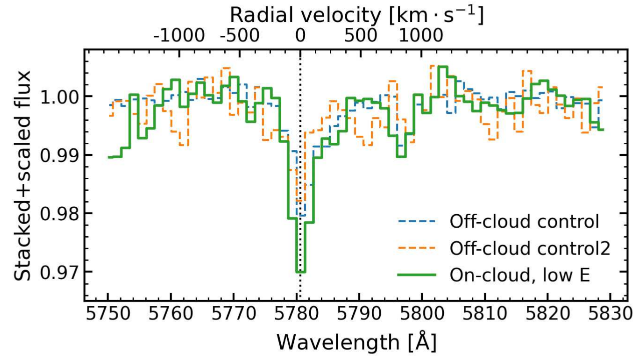

Figure 11. Stacked spectra of O- and B-type stars from three selected regions shown in Figure 10. Each spectrum was normalized by its continuum prior to stacking. The green solid line represents the stacked spectra of stars in the cloud region, while blue and orange dashed lines show the stacked spectra from off-cloud control regions. The black dotted vertical line indicates the DIB $\lambda 5780$ air wavelength of 5780.61 Å (Hobbs et al. 2009).

Note that both line-of-sight velocity in GSR (Galactic Standard of Rest reference frame) and equivalent width are in a roughly increasing sequence along the pattern, which may indicate that the high-velocity DIB structure does have some extent of thickness along the $(l, b) = (155, -5)^\circ$ sight line. The gradient of velocity in the structure is not very evident, ranging from about 200 to 250 km s^{-1} in GSR when moving outward. Equivalent widths detected by stellar spectra down the stripe rise from about 0.3 to 1.1, meaning that the light of background stars at further distance goes through thicker DIB clouds or diffuse medium, generating DIB features. However, this does not mean that this positive velocity HV-DIB clump truly extended from 1 to 5 kpc as we observe in Figure 12, since the asymmetric distribution of distance error of Gaia can elongate the structure along the line of sight and cause the artificial shape of the cloud (Bailer-Jones et al. 2021).

6. Conclusion

In this paper, we have analyzed the distance of the HVC ACS. We used interstellar extinction calculated on K-giant stars with LAMOST atmospheric parameters, 2MASS photometry, and Gaia distance, and used the DIB feature at 5780 Å with LAMOST low-resolution spectra to support as our cloud tracers.

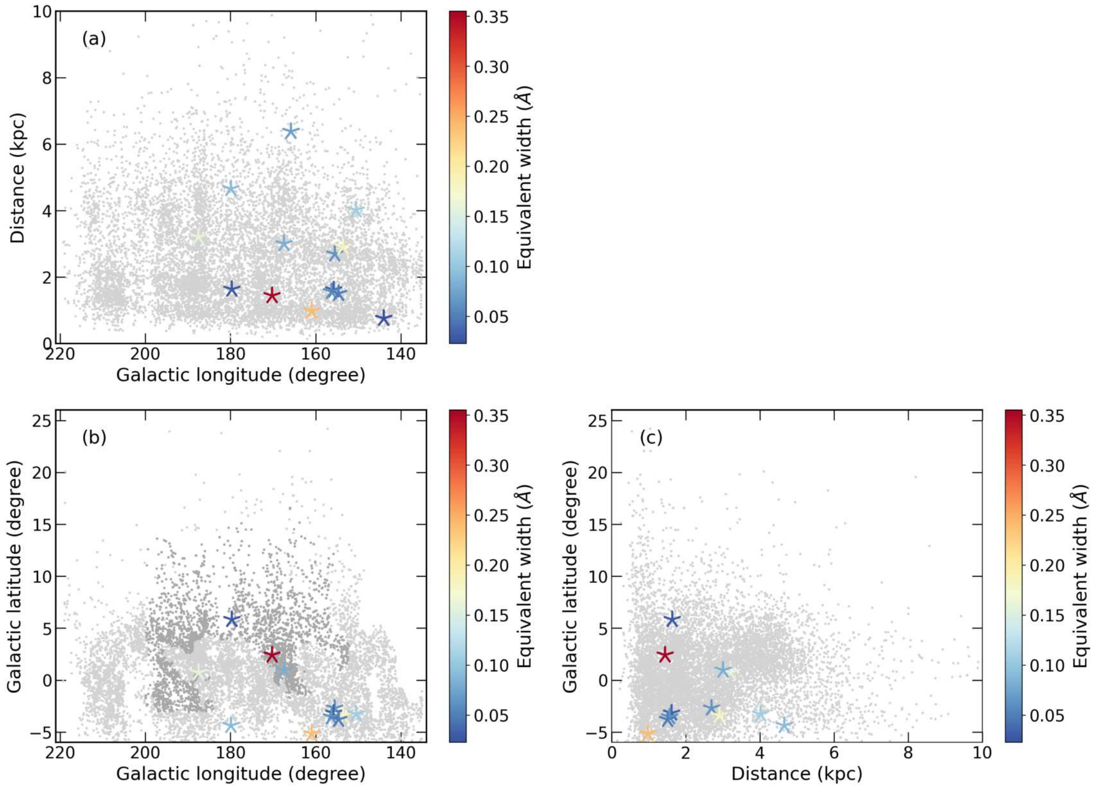

Figure 12. Three-dimensional positions of HV-DIBs with positive velocity. We used the distance of our O- and B-type star tracers accomplished by Bailer-Jones et al. (2021). HV-DIBs are color-coded by their equivalent widths. Light gray dots on the background show all reliable DIB measurements, and dark gray dots in (b) emphasize the cloud area. DIBs at $(l, b) = (155, -5)^{\circ}$ show clustering characteristics in all three plots, clumpy-shaped in the glon-glat plot and bar-shaped in plots relevant to distance.

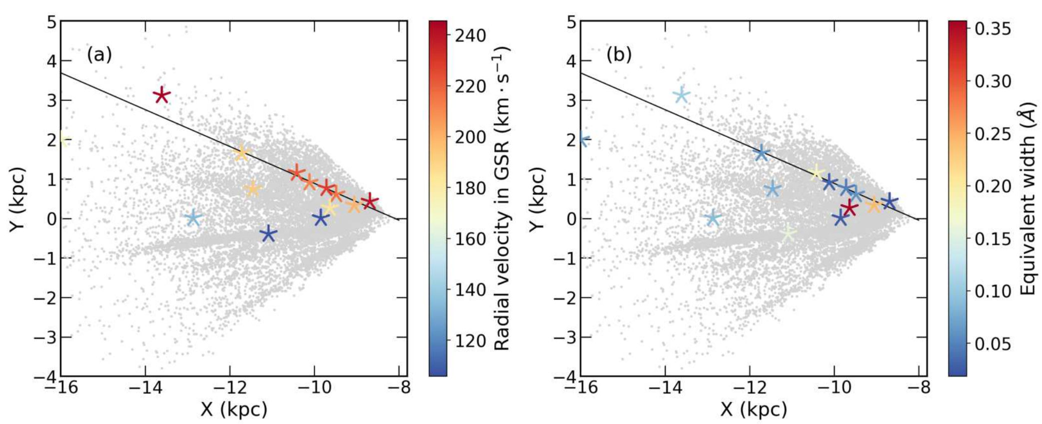

Figure 13. High-quality positive velocity HV-DIBs (Asterisks color-coded in velocity and equivalent width) in the *X*–*Y* plane. Gray dots denote all reliable DIB measurements. The angular position of the structure at $(l, b) = (155, -5)^{\circ}$ is emphasized with the black solid line.

In both methods, the signal of ACS is too weak to be found. In the extinction method, we compared the extinction variation of on- and off-cloud stars, but no excess extinction independently appeared in the on-cloud curve that we displayed. With the DIB method, it was possible for us to identify the cloud in velocity space. We should have discovered a component with an anomaly line-of-sight velocity in the LSR of about $-100\,\mathrm{km\ s^{-1}}$ if ACS was in the detectable range of our O- and B-type star tracers. But no prominent structure with negative velocity incompatible with the disk was uncovered in the Galactic longitude-radial velocity plot.

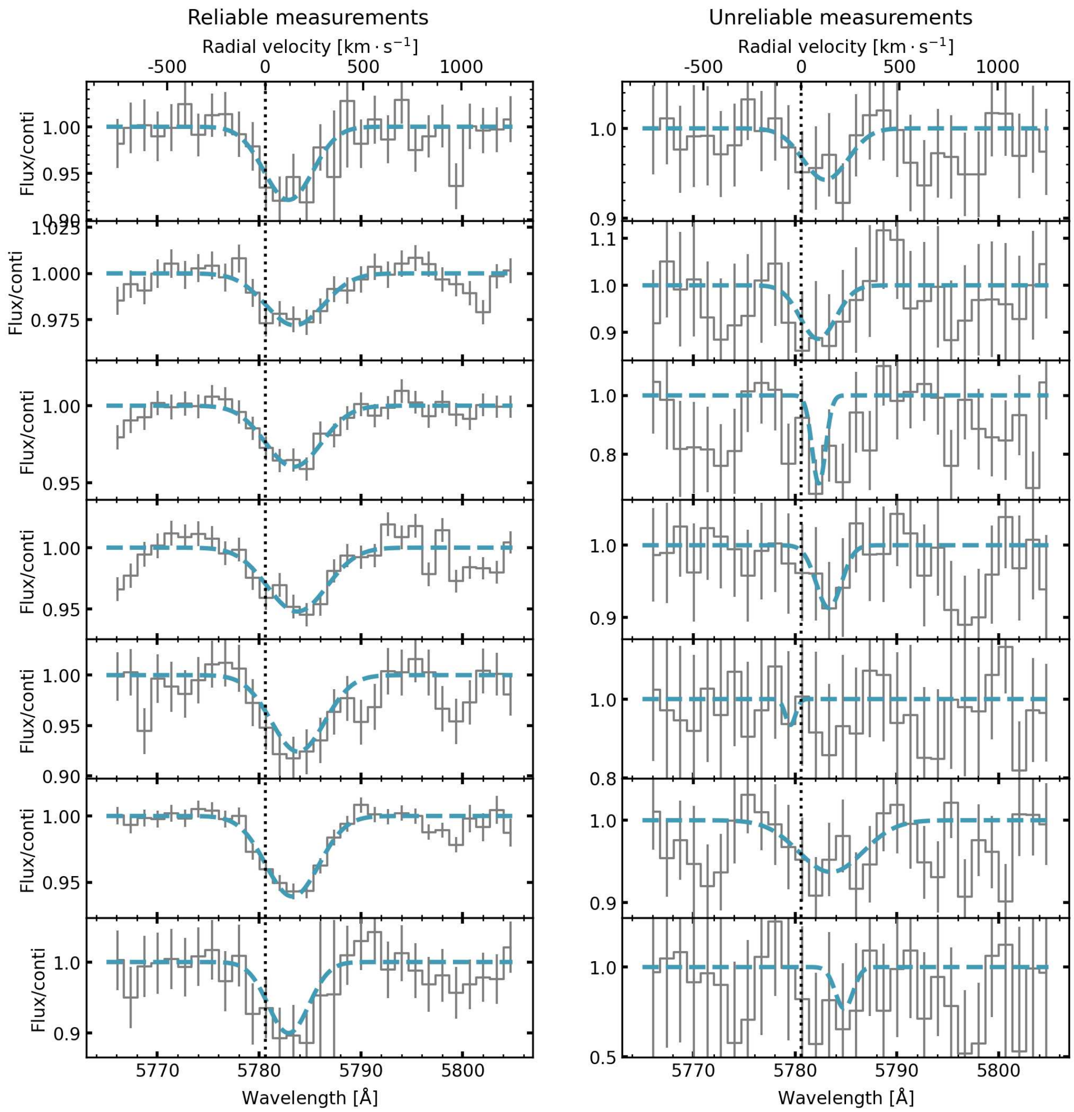

Figure 14. Spectra and fitting results for stars with positive velocity HV-DIB detections. We mark the central air wavelength of DIB λ5780 in the rest frame with a black dotted line, which is 5780.61 Å measured by Hobbs et al. (2009). The gray solid lines denote the observed spectra, while green dashed lines represent the Fitted Gaussian model. We performed an eye check and plotted some of the reliable measurements on the left side and unreliable ones on the right side.

Both analyses indicate that nowadays, data is still incapable of detecting the ACS. The most intuitive explanation is that the cloud is even further than our tracers, which can lead us to give a distance lower limit of ∼8 kpc. Smoker et al. (2011) also measured the distance to ACS using the absorption-line method. They owned two tracer stars possessing ultraviolet band spectra, HDE 248894 and HD 256725, but failed to identify the absorption by ACS as well, and gave a lower limit of 8 kpc. The distances of HDE 248894 and HD 256725 can be updated to 2.8 and 4.0 kpc from Bailor-Jones' distance estimation based on Gaia EDR3 (Bailer-Jones et al. 2021) now. So their lower limit should be altered to ∼4 kpc, and our work pushes the lower limit to ∼8 kpc, which means the ACS might have a Galactocentric distance of over 16 kpc. Other explanations for our non-detection might be that: (1) the signal of the ACS can be concealed by the strong affection of the Galactic disk; (2) the neutral hydrogen and dust in the ACS are not sufficient to cause a remarkable extinction excess.

The future direction of this study includes improving the number, spatial scale, and measurement quality (accuracy/resolution) of stellar distance and gaining deeper stellar spectrum observations. Besides, we can study more about the physical nature of HVCs (e.g., their correlation with dust) to look for new detection methods.

Acknowledgments

The authors appreciate discussions with Jiadong Li.

We acknowledge the support of the National Key R&D Program of China No. 2019YFA0405500 and the China Manned Space Project No. CMS-CSST-2021-A08.

We acknowledge the support of the National Natural Science Foundation of China (NSFC) under grant Nos. 12041305, 12173016.

We acknowledge the Program for Innovative Talents, Entrepreneur in Jiangsu.

We acknowledge the science research grants from the China Manned Space Project with Nos.CMS-CSST-2021-A08 and CMS-CSST-2021-A07.

This work used the data from the European Space Agency (ESA) mission Gaia (https://www.cosmos.esa.int/gaia), processed by the Gaia Data Processing and Analysis Consortium (DPAC; https://www.cosmos.esa.int/web/gaia/dpac/consortium). Funding for the DPAC has been provided by national institutions, in particular the institutions participating in the Gaia Multilateral Agreement.

Guo Shou Jing Telescope (the Large Sky Area Multi-Object Fiber Spectroscopic Telescope, LAMOST) is a National Major Scientific Project built by the Chinese Academy of Sciences. Funding for the project has been provided by the National Development and Reform Commission. LAMOST is operated and managed by the National Astronomical Observatories, Chinese Academy of Sciences.

Facilities: Gaia, LAMOST.

Software: `IPython` (Pérez & Granger 2007), `jupyter` (Kluyver et al. 2016), `pandas` (The pandas development team 2020), `Astropy` (Astropy Collaboration et al. 2022), `numpy` (Harris et al. 2020), `scipy` (Virtanen et al. 2020), `matplotlib` (Hunter 2007).

Appendix
Uncertainty Estimation of the Extinction Method

In this section, we will describe how we estimate the uncertainties that might appear in the extinction method. The comprehensive uncertainty estimation includes the uncertainty of the bluest edge, the observational uncertainty of distance measurement, J-band and K_S-band photometry, and the emerged Poisson error when binning the data into sight line and distance bins.

A.1. The Uncertainty of the Bluest Edge

The uncertainty of the blue edge is made up of systematic uncertainty arising from metallicity and age variations of the star sample, and observational uncertainty involved.

First, we examined the temperature-intrinsic color relation for K giants provided by the PARSEC models (Bressan et al. 2012; Chen et al. 2014, 2015; Tang et al. 2014; Marigo et al. 2017; Pastorelli et al. 2019, 2020). Using PARSEC 1.2 s isochrones with ages ranging from 2 to 13.7 Gyr (According to the SFH of Galactic disk from Nataf et al. 2024), metallicities from -1 to 0.5, and a label of 3 (Red Giant Branch stage), we found that the broadening in the temperature-intrinsic color relation in the 2MASS J and K_s bands due to age and metallicity variations is approximately 0.04 mag. This value gives a glimpse of the systematic error caused by the metallicity and age variation of K giants.

We also attempted to measure the bluest edge in different metallicity bins for our LAMOST DR5 K giants, using a modified version of the method outlined in Jian et al. (2017) and Cao et al. (2024). We binned the stars by metallicity (width 0.15 dex, -1 to 0.5 dex; except for the bin of stars with poorest metallicity, for which we chose it to be -1.0 to -0.7 to guarantee enough stars) and effective temperature $T_{\rm eff}$ (width $\sim$50 K, excluding bins with fewer than 100 stars). To find the bluest edge, we iteratively selected the 5% bluest stars ($J - K_S$ color in 2MASS bands) in each temperature bin, fitted their color-temperature relation using Random Forest Regressor (RFR), and removed outliers exceeding 3σ uncertainty (combining the photometric uncertainties in J and K_S bands, and the uncertainty from LAMOST effective temperature, $\sim$0.030 mag according to Jian et al. 2017). The obtained bluest edges for different metallicity bins are plotted in Figures A1 and A2 below. However, the observed variations in the bluest edge with metallicity were significantly larger than those predicted by the PARSEC models above, which is $\sim$0.1 mag versus $\sim$0.04 mag. According to Jian et al. (2017), this discrepancy likely additionally arises from the choice of fraction of the bluest stars (the method), Poisson noise, and observational errors in photometry, temperature, and metallicity. Jian et al. (2017) estimated that the different blue fraction will introduce an error of about 0.02 mag.

So, we further estimated the uncertainty of the blue edges contributed by Poisson noise and observational errors in temperature and metallicity with the Monte Carlo method. The photometric and $T_{\rm eff}$ value of the bluest fraction are recalculated 1000 times by the Monte Carlo method: each new value is the sum of the catalog value and a Gaussian random number determined by its observational error. We selected the metallicity bins [-1.0, 0.7), [-0.55, -0.4), [-0.25, -0.1), and [0.35, 0.5) to represent a quick estimate of the uncertainty provided by Poisson noise and observational errors over different metallicity ranges. We obtained that the blue edge uncertainties of the metallicity bins [-1.0, 0.7), [-0.55, -0.4), [-0.25, -0.1), and [0.35, 0.5) are 0.0198, 0.0045, 0.0029, and 0.0051 mag on average of the whole $T_{\rm eff}$ range, respectively. Noted that when we calculated the average uncertainty for the [Fe/H] bin [0.35, 0.5), we dropped the points with $T_{\rm eff} < 4350$ K, for the star counts in those $T_{\rm eff}$ bins are smaller than 100. Blue edges for the metallicity bins [-1.0, 0.7), [-0.55, -0.4), [-0.25, -0.1), and [0.35, 0.5) with Monte

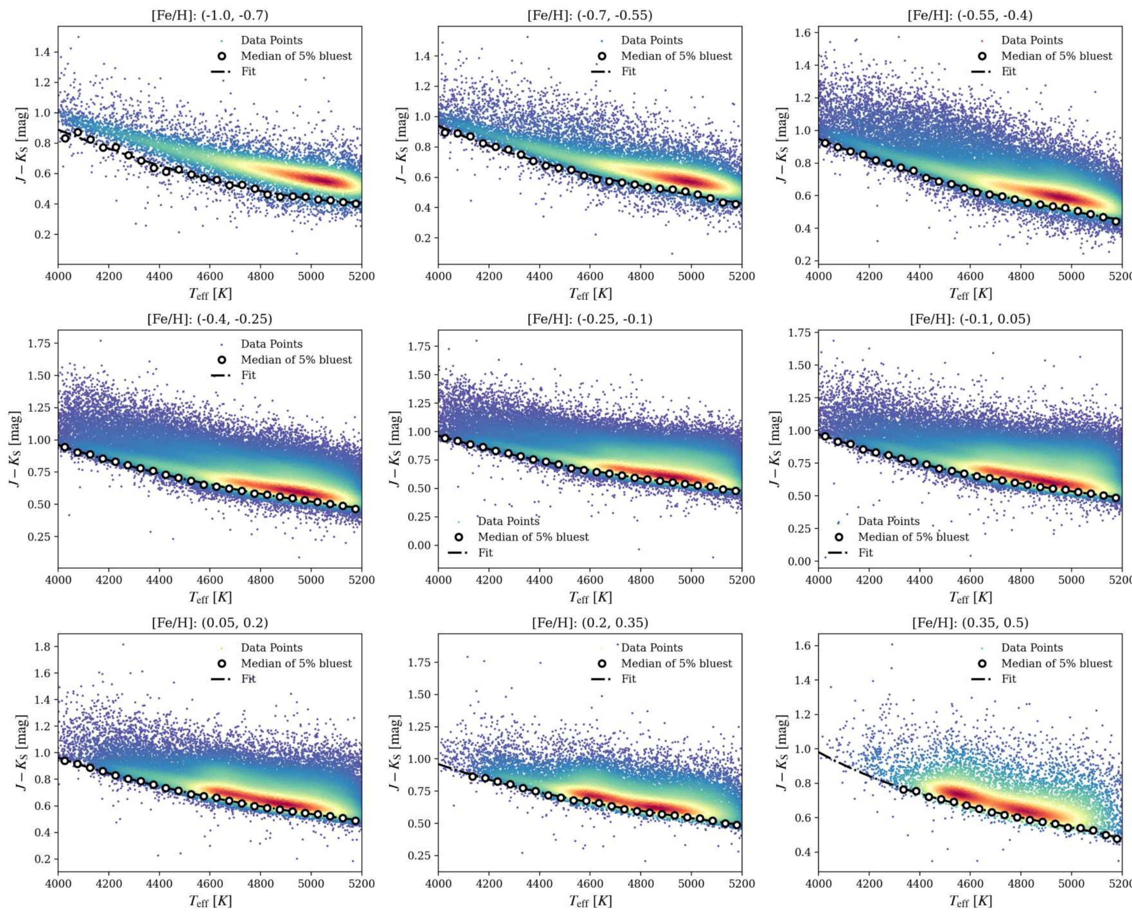

Figure A1. Blue edges calculated from the new iterative method for the metallicity bins [Fe/H] [−1.0, −0.7), [−0.7, −0.55), [−0.55, −0.4), [−0.25, −0.1), [−0.1, 0.05), [−0.05, 0.2), [0.2, 0.35), [0.35, 0.5]. Data points in different metallicity bins are plotted with color-coded solid dots, with the color map denoting the Gaussian KDE density map of the points. The iteratively selected blue edge points are drawn with black circles. We also plot the polynomials fitted to the blue edge points with black dotted-dashed lines.

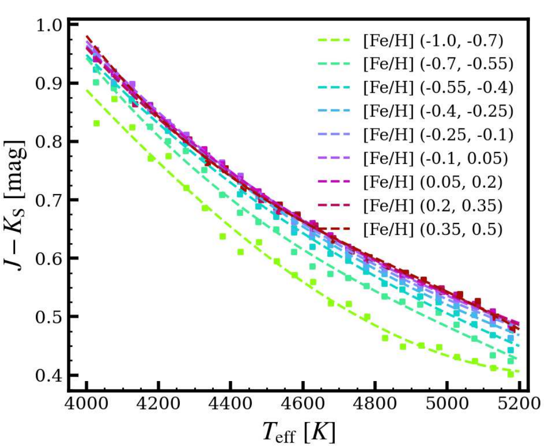

Figure A2. All the resulting blue edges in one plot. The square dots are the selected blue edge points, while the dashed lines denote the fitted polynomials to them.

Carlo uncertainties are plotted in Figure A3. For the whole sample with metallicity falling in the range [−1.0, 0.5], its Monte Carlo uncertainty is plotted in Figure A4, which is only about 0.002 mag.

In Figure A5, we compare the dispersion of the effective temperature-intrinsic color relation for RGB stars in PARSEC 1.2 s with those computed for different metallicity bins in Figure A2. Overall, the systematic error caused by the different blue fraction is 0.02 mag (according to Jian et al. 2017), and the systematic error caused by the variation of age and metallicity is ∼0.04 mag (according to PARSEC). For the uncertainties caused by the Poisson error and observational errors, it will range from ∼0.003 to ∼0.020 mag if we bin the metallicity, and it will be ∼0.002 mag if we use the whole sample. In the main text, we applied the bluest edge calculated by the whole sample with [Fe/H] ranging from −1.0 to 0.5, so the overall uncertainty of the bluest edge is ∼0.045 mag.

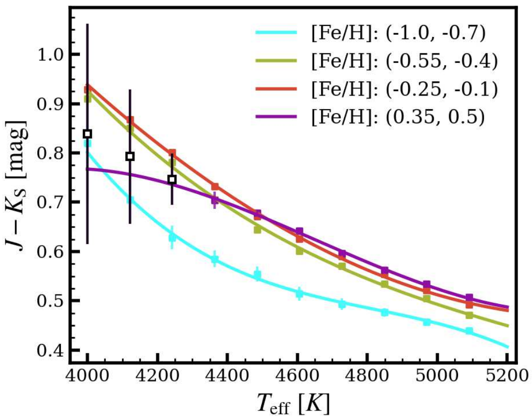

Figure A3. The Monte Carlo errors calculated for four different metallicity bins. In the formal determination of the blue edge of the metallicity bin [0.35, 0.5], the blue edge points with $T_{\rm eff} < 4350$ K are discarded due to the small number of data points.

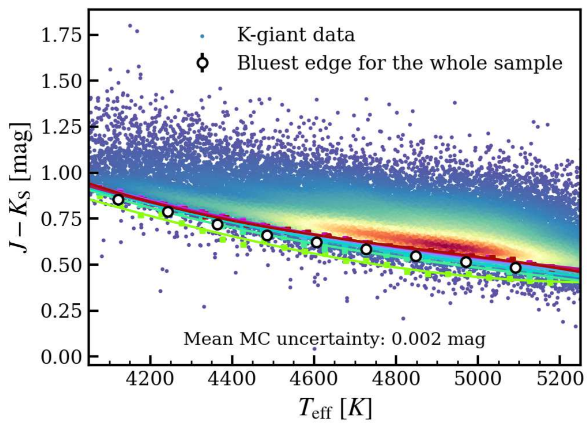

Figure A4. The blue edge point and Monte Carlo errors calculated for the whole sample with $-1.0 < [\mathrm{Fe/H}] < 0.5$. The mean Monte Carlo uncertainty over the whole temperature range is $\sim$0.002 mag. The blue edges computed for different metallicity bins in Figure A2 are also drawn for reference.

A.2. The Uncertainty Caused by the Observation and the Poisson Error

For the observational uncertainty of distance measurement, J-band and K_S-band photometry, we can account for them with the Monte Carlo technique to transfer the uncertainties of the observables to the final distance-extinction relation. The number of stars N in each distance and sight line bin also has Poisson statistical fluctuations, leading to additional uncertainty in the mean extinction. However, in each Monte Carlo simulation, stars may be assigned to different bins due to those observational errors, and this change in assignment indirectly reflects the statistical fluctuation of the number of stars in each bin (Poisson error). Therefore, we do not need to calculate it separately, it is already included in the simulation

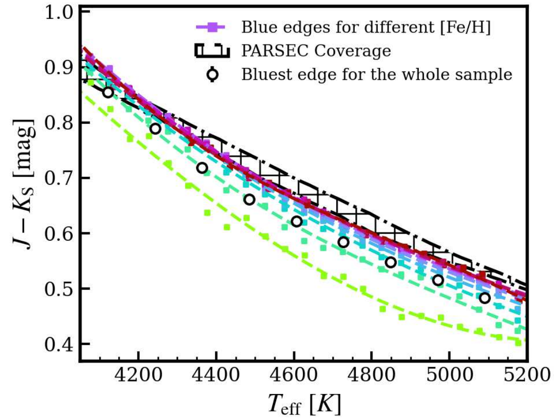

Figure A5. The dispersion of effective temperature-intrinsic color relation for RGB stars in PARSEC 1.2 s. We select stars with logAge from 9.3 to 10.13, metallicity [M/H] from -1 to 0.5 in PARSEC. Meanwhile, we plot the blue edges computed for different metallicity bins in Figure A2, and the blue edge point and Monte Carlo errors calculated for the whole sample with $-1.0 < [\mathrm{Fe/H}] < 0.5$ for better comparison.

process. Similarly to the last section, the distance, photometric, and $T_{\rm eff}$ value of the bluest fraction are recalculated 1000 times by the Monte Carlo method: each new value is the sum of the catalog value and a Gaussian random number determined by its observational error. Then we can obtain 1000 realizations of the distance-extinction relation, and determine their 16, 50, 84 percentiles. The overall uncertainty can be calculated for each distance and sight line bin as:

$$\sigma_{\rm total} = \sqrt{\sigma^2_{\rm BluestEdge} + \sigma_{\rm MonteCarlo}} \tag{A1}$$

ORCID iDs

Yu-Ting Wang (王雨亭) https://orcid.org/0009-0007-8574-0890
Chao Liu (刘超) https://orcid.org/0000-0002-1802-6917
Zhi-Yu Zhang (张智昱) https://orcid.org/0000-0002-7299-2876

References

Astropy Collaboration, Price-Whelan, A. M., Lim, P. L., et al. 2022, ApJ, 935, 167
Bailer-Jones, C. A. L., Rybizki, J., Fouesneau, M., Demleitner, M., & Andrae, R. 2021, AJ, 161, 147
Bressan, A., Marigo, P., Girardi, L., et al. 2012, MNRAS, 427, 127
Cao, Z., Jiang, B., Wang, S., & Li, J. 2024, AJ, 168, 256
Chen, Y., Bressan, A., Girardi, L., et al. 2015, MNRAS, 452, 1068
Chen, Y., Girardi, L., Bressan, A., et al. 2014, MNRAS, 444, 2525
Clemens, D. P. 1985, ApJ, 295, 422
Cui, X.-Q., Zhao, Y.-H., Chu, Y.-Q., et al. 2012, RAA, 12, 1197
Davies, R. D. 1972, Natur, 237, 88
Draine, B. T. 2003, ARA&A, 41, 241
Ducati, J. R., Bevilacqua, C. M., Rembold, S. B., & Ribeiro, D. 2001, ApJ, 558, 309
Freudenreich, H. T., Berriman, G. B., Dwek, E., et al. 1994, ApJL, 429, L69
Harris, C. R., Millman, K. J., van der Walt, S. J., et al. 2020, Natur, 585, 357

Heiles, C. 1979, ApJ, 229, 533
Herbig, G. H. 1995, ARA&A, 33, 19
HI4PI Collaboration, Ben Bekhti, N., Flöer, L., et al. 2016, A&A, 594, A116
Hobbs, L. M., York, D. G., Thorburn, J. A., et al. 2009, ApJ, 705, 32
Hunter, J. D. 2007, CSE, 9, 90
Jian, M., Gao, S., Zhao, H., & Jiang, B. 2017, AJ, 153, 5
Kluyver, T., Ragan-Kelley, B., Pérez, F., et al. 2016, Jupyter Notebooks—a publishing format for reproducible computational workflows (Amsterdam: IOS Press), 87
Lan, T.-W., Ménard, B., & Zhu, G. 2015, MNRAS, 452, 3629
Lehner, N., & Howk, J. C. 2010, ApJ, 709, L138
Lehner, N., Howk, J. C., Marasco, A., & Fraternali, F. 2022, MNRAS, 513, 3228
Lehner, N., Keenan, F. P., & Sembach, K. R. 2001, MNRAS, 323, 904
Liu, C., Deng, L.-C., Carlin, J. L., et al. 2014, ApJ, 790, 110
Marasco, A., Fraternali, F., Lehner, N., & Howk, J. C. 2022, MNRAS, 515, 4176
Marigo, P., Girardi, L., Bressan, A., et al. 2017, ApJ, 835, 77
Muller, C. A., Oort, J. H., & Raimond, E. 1963, CRAS, 257, 1661
Nataf, D. M., Schlaufman, K. C., Reggiani, H., & Hahn, I. 2024, ApJ, 976, 87
Pastorelli, G., Marigo, P., Girardi, L., et al. 2019, MNRAS, 485, 5666
Pastorelli, G., Marigo, P., Girardi, L., et al. 2020, MNRAS, 498, 3283
Peek, J. E. G., Bordoloi, R., Sana, H., et al. 2016, ApJL, 828, L20
Pérez, F., & Granger, B. E. 2007, CSE, 9, 21
Ryans, R. S. I., Keenan, F. P., Sembach, K. R., & Davies, R. D. 1997, MNRAS, 289, 83
Schwarz, U. J., Wakker, B. P., & van Woerden, H. 1995, A&A, 302, 364
Sembach, K. R., Savage, B. D., Shull, J. M., et al. 2000, ApJL, 538, L31
Sembach, K. R., Wakker, B. P., Savage, B. D., et al. 2003, ApJS, 146, 165
Skrutskie, M. F., Cutri, R. M., Stiening, R., et al. 2006, AJ, 131, 1163
Smoker, J. V., Fox, A. J., & Keenan, F. P. 2011, MNRAS, 415, 1105
Smoker, J. V., Lynn, B. B., Christian, D. J., & Keenan, F. P. 2006, MNRAS, 370, 151
Tang, J., Bressan, A., Rosenfield, P., et al. 2014, MNRAS, 445, 4287
The pandas development team, 2020 pandas-dev/pandas: Pandas 1.0.3,
Thom, C., Peek, J. E. G., Putman, M. E., et al. 2008, ApJ, 684, 364
Thom, C., Putman, M. E., Gibson, B. K., et al. 2006, ApJL, 638, L97
Tripp, T. M., & Song, L. 2012, ApJ, 746, 173
Verschuur, G. L. 1969, ApJ, 156, 771
Virtanen, P., Gommers, R., Oliphant, T. E., et al. 2020, NatMe, 17, 261
Wakker, B. P. 1991, A&A, 250, 499
Wakker, B. P. 2001, ApJS, 136, 463
Wakker, B. P., & van Woerden, H. 1997, ARA&A, 35, 217
Wakker, B. P., York, D. G., Howk, J. C., et al. 2007, ApJL, 670, L113
Wakker, B. P., York, D. G., Wilhelm, R., et al. 2008, ApJ, 672, 298
Wang, S., & Chen, X. 2019, ApJ, 877, 116
Wang, S., & Jiang, B. W. 2014, ApJL, 788, L12
Wang, S., Zhang, C., Jiang, B., et al. 2020, A&A, 639, A72
Westmeier, T. 2018, MNRAS, 474, 289
Xiang, M., Rix, H.-W., Ting, Y.-S., et al. 2021, ApJS, 253, 22
Xu, Y., Hao, C. J., Liu, D. J., et al. 2023, ApJ, 947, 54
Xu, Y., Liu, C., Tian, H., et al. 2020, ApJ, 905, 6
Xue, M., Jiang, B. W., Gao, J., et al. 2016, ApJS, 224, 23
Yan, Q.-Z., Yang, J., Su, Y., et al. 2021, ApJ, 922, 8
Yan, Q.-Z., Zhang, B., Xu, Y., et al. 2019, A&A, 624, A6
Zhang, B., Liu, C., & Deng, L.-C. 2020, ApJS, 246, 9
Zhao, H., Schultheis, M., Recio-Blanco, A., et al. 2021, A&A, 645, A14
Zucker, C., Speagle, J. S., Schlafly, E. F., et al. 2019, ApJ, 879, 125